Study of hourglass-shaped specimens for the analysis of compression behaviour in fibre direction of FRP composites using compression and four-point bending tests

A.Cocchi[a,*], O. Montagnier[b], C. Hochard[a]

[a] *Aix Marseille Univ, CNRS, Centrale Marseille, LMA UMR 7031, 4 Impasse Nikola Tesla, 13453 Marseille Cedex 13, France*

[b] *Centre de Recherche de l'Ecole de l'Air, CReA, B.A. 701, 13661 Salon-Air, France*

Abstract

Flat hourglass specimens are proposed to assess the compressive behaviour of FRP utilizing two testing techniques. The hourglass shape helped to ensure failure at the centre of the specimen and to minimize in-plane stress concentration in this zone. Four-point bending tests are carried out and measures are performed via DIC. A procedure to calculate bending moment is proposed and validated in presence of large displacements. To evaluate the specimen and the method proposed, two different materials were tested, an E-glass/Epoxy unbalanced woven and a Carbon/PEEK balanced woven. In a second time ASTM D695 compression tests are carried out on the E-Glass/Epoxy composite to compare the hourglass specimens to the standardized dog-bone. The two testing techniques are analysed and compared.

Keywords: Glass fibres, Failure, Mechanical testing, Finite element analysis (FEA)

1. Introduction

Determination of compression properties of composite materials is a difficult task. As reported by multiple authors [1–4] standard tests tend to underestimate compression strength of composites materials. These premature failures are mainly due to stress concentrations at the load introduction zones or, sometimes, uncontrolled buckling of the specimen. With modern day necessity to reduce weight in composites applications, an underestimation of compression properties can lead to overly conservative designs.

Many testing methods to characterize the compressive properties of composite materials can be found in literature. In the case of pure compression tests on constant cross-section specimens, standards like ASTM D3410 prescribe shear loading. In this case failure generally takes place near the tabs where the concentration of compressive and shear stress are maximum [5]. In end compression tests (standard or modified ASTM D-695), specimens have rectangular or dog-bone shape and anti-buckling fixtures are used. In these tests failure generally occurs at the ends of the rectangular specimens or just after the connection radius of the dog-bone specimen, a zone of sharp cross-section variation introducing a stress concentration.

In bending, failure usually occurs at the load point rather than supports due to the high stress concentration and high compressive stress in the material under the loading nose [6, 7]. A solution to avoid this kind of premature failure is to perform hinged buckling tests [8–11], which ensures failure in the middle of the specimen where the bending moment is at its maximum. However, the imposed moment and the stress state generate in the coupon depend on its deformed configuration.

*Corresponding Author: Aldo Cocchi, LMA UMR 7031, 4 Impasse Nikola Tesla 13453 Marseille Cedex 13

Email addresses: cocchi@lma.cnrs-mrs.fr (A.Cocchi), olivier.montagnier@ecole-air.fr (O. Montagnier), hochard@lma.cnrs-mrs.fr (C. Hochard)

Another solution to ensure failure away from the load introduction zones is to use waisted coupons with a smaller cross-section in the central zone whilst limiting the stress concentration generated by the cross-section variation. This technique has been used in tension on flat specimens with a large radius of curvature in the gauge zone to ensure a gradual cross-section variation [12, 13]. The radius of curvature is of the order of one meter and ensures failure at the centre of the specimen while guaranteeing an extremely low stress concentration. This geometry is described by Payan [13] and also adopted by De Baere *et al.* [12] and more recently by Öztürk *et al.* [14]. The authors refer to this shape as 'dumbbell' and 'dogbone' but this nomenclature is also used for common specimens with a central constant cross-section. To put emphasis on the constant curvature radius in the central part of the specimen, we will refer to the shape as 'hourglass'.

In this paper, –specimens with this type of geometry are proposed for an ASTM D695 compression test and a four-point bending test. It should be noted that in the literature there are also specimens that present a smooth waisted section but in thickness to ensure failure away from the load introduction zones. For example, Wisnom [15] has proposed waisted specimens with in-thickness plies drop-off for tensile purposes. Similarly, the authors have proposed tubular coupons with in-thickness plies-drop-off for tension and compression tests [16–18].

In this work, first of all, results obtained in tension tests are presented. Afterwards, we explain the design of a flat hourglass shaped specimen well-adapted for compression and four-point bending tests. Next, bending tests are presented and analysed using a geometrical protocol to estimate bending moment taking into account large rotations and displacements. An unbalanced satin woven E-Glass/Epoxy and a balanced satin woven Carbon/PEEK prepreg composites are tested to validate the protocol. Then, compression test are performed on a fixture conform to ASTM D695 using standard specimens and an adapted shorter version of the hourglass specimens. Only the E-Glass/Epoxy composite is tested in compression. Finally, results are presented and analysed.

2. Coupons preparation and tensile test

In this paper, two different materials are considered. The first one is an E-glass fibre reinforced epoxy produced by Hexcel (M42ST/1055) 5-harness satin weave. The main characteristic of this woven is to be unbalanced with 83% of the fibres in warp direction and only 17% in weft. Press moulding at 150°C for 5h at a pressure of 5 bar is the recommended cure cycle. Due to impossibility to perform press moulding process, we opted for autoclave consolidation and increased pressure to 7 bar. Coupons were water-jet cut from plates with a ply thickness of 0.33 mm for an average fibre volume fraction of 48%. The second one is a Carbon/PEEK balanced woven composite (T300J, PiPreg 3106-1250P0378). Specimens were cut via water-jet from plates consolidated by press moulding at 400°C with a cured ply thickness of 0.28 mm.

To begin, tensile tests were carried-out on $[0°]_8, [90°]_8, [45°, -45°]_8$ E-glass/Epoxy specimens to assess the material tensile properties in longitudinal, transverse and shear directions. Specimens were shaped according to the geometry depicted in Figure 1 [12, 13], the dimensions of this specimen come from the adaptation of a $300 \times 30\,mm^2$ rectangular tabbed specimen. To position the specimen in the machine grips, a $50 \times 30\,mm^2$ rectangular zone was left at each extremity of the coupon. Consequently the length of the waisted central part was fixed to 200 mm, a ratio of 2/3 between the width at the extremities (30 mm) and at the centre (20 mm) was chosen, this resulted in a constant radius of 1002 mm in the waisted part. The described shape ensures failure in the central zone of the coupon, avoiding premature ends failure. On the other hand, the radius is sufficiently large so that only a very limited in-plane stress concentration is generated in this central zone as depicted in Fig. 2a. The stress concentration generated in tension by the geometry depicted in Fig. 1 was estimated simulating the specimen on FEM software ABAQUS. The coupon was simulated as a 3D orthotropic solid of thickness 1 mm meshed with C3D6 elements and engineering constants reported in Tab. 1. A load of 2000 N, corresponding to a nominal stress (σ_{nom}) of 100 MPa for the $20 \times 1\,mm^2$ central cross-section, was imposed on one end of the coupon while the other was fixed. Stress distribution in the section of minimal width is depicted in Fig. 2b. In this article we define the in plane stress concentration coefficient of a coupon (S_{coupon}) as the ratio between the maximum stress in fibre direction (σ_{MAX}) and the nominal stress:

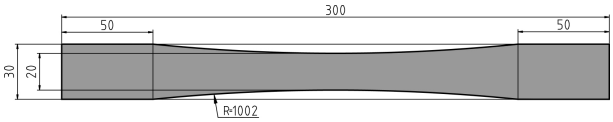

Figure 1: Flat hourglass shaped specimen used for traction and fatigue testing (dimensions in mm) [12, 13]

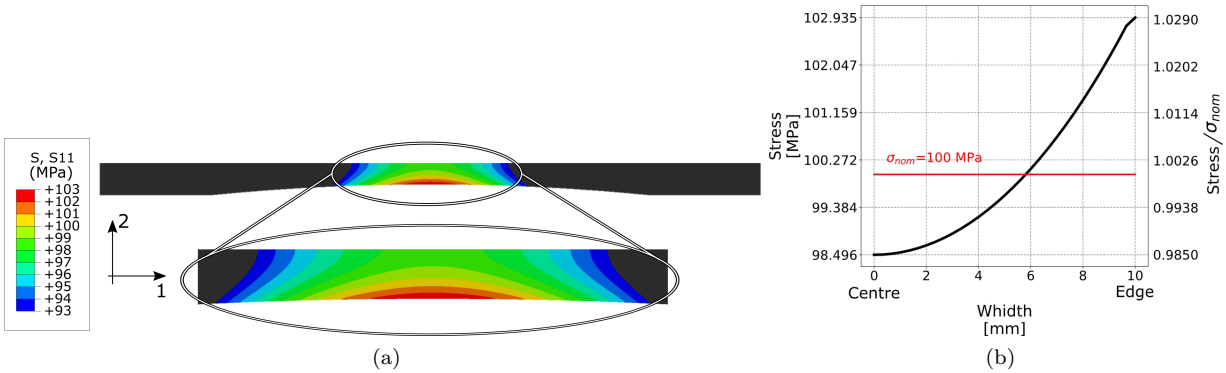

Figure 2: Tensile test simulation: a) stress field on a large flat hourglass shaped specimen for a nominal stress of 100 MPa; b) stress distribution generated by the hourglass shape at the centre of the specimen

$$S_{coupon} = \frac{\sigma_{MAX}}{\sigma_{nom}} \tag{1}$$

In the present case of an hourglass coupon with a curvature radius of 1002 mm in tension, the coefficient $S_{hourglass\_T}$ is equal to 1.029 (Fig. 2b).

Tests were carried out on an MTS1000 universal testing machine at a constant displacement rate of 1 mm/min. Two specimens were tested for each layup for a total of six specimens. Figure 3a shows tensile behaviour in fibre's direction. Failure in warp direction was brittle and occurred, as expected, at the centre of the specimens, $[0°]_8$ coupons failed at 750 ± 8 MPa for a strain of $2.59 \pm 0.03\%$. Observed behaviour is slightly non-linear due to damage generated in the 17% of fibres in weft direction as described in [19]. For $[90°]_8$ samples (Fig. 3b), failure also occurred at the centre of the coupon at 146 ± 5 MPa for a strain of $2.15 \pm 0.07\%$. Transverse and shear direction behaviours (Figs. 3b and 3c), are strongly non-linear due to damage and plasticity in matrix. For simulation purpose, only the linear part of the material constitutive equation in transverse and shear direction was taken into account (see red lines on the figures). The three orientations made possible to identify engineering constants as reported in Table 1.

A single tensile test on a $[0]_8$ balanced woven carbon/PEEK specimen was carried out as we are not interested in the full determination of the material's engineering constants. The hourglass geometry of Fig. 1 was utilized and the specimen failed once again at its centre. The result of the test is depicted in Fig. 4. Behaviour in 0° direction is linear until failure that occurred at 920 MPa for a strain of 1.55 %. Young's Modulus is measured at a value of 55 GPa.

E_{11}	E_{22}	G_{12}	G_{13}*	G_{23}*	ν_{12}	ν_{13}*	ν_{23}*
MPa	MPa	MPa	MPa	MPa	-	-	-
30730	13535	3870	3870	3870	0.25	0.25	0.25

Table 1: Unbalanced woven E-glass/Epoxy (M42ST/1055) engineering constants determined via tensile testing (values with star (*) are estimated from the quasi-unidirectional behaviour of the woven and used only for FEM simulation)

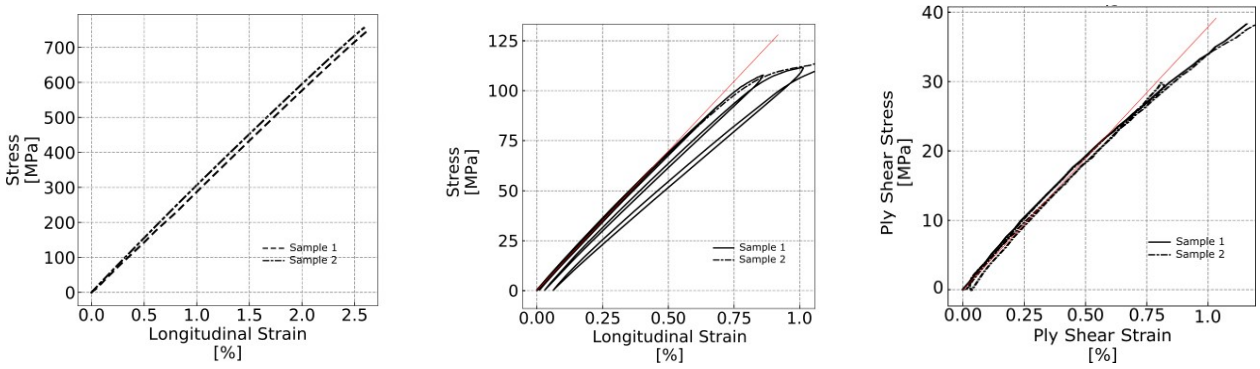

Figure 3: Tensile test on E-glass/Epoxy specimens ($V_f = 0.48$): a) $[0]_8$ layup; b) $[90]_8$ layup, c) $[45, -45]_{4S}$ layup

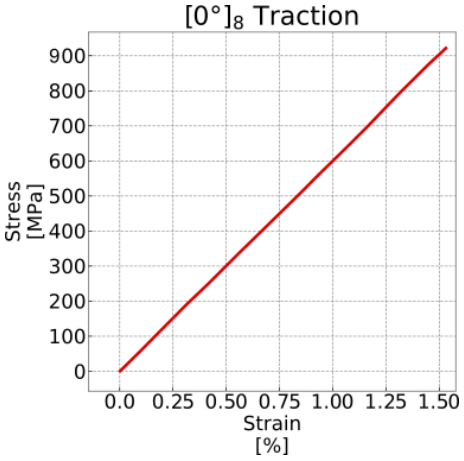

Figure 4: Tensile test on $[0]_8$ balanced woven Carbon/PEEK specimen

3. Definition of hourglass geometry for compression and bending tests

It was chosen to adopt the hourglass shape for the specimens to test in bending and compression to ensure failure at the centre of the coupons. An adapted hourglass coupon was designed starting from the one utilized in tension [12, 13] (Fig. 1). Its dimensions were adjusted for usage in four-point bending and end-loading compression. The total length of the specimen was fixed to 80 mm as per the standardized dog-bone coupon for the ASTM D695 end-loading compression test (Fig. 5a). The length of the waisted part was fixed at 75 mm to leave a small straight part between the ends and the waisted part. It was chosen to keep the same ratio of *2/3* between the maximum and minimum width as in the tension hourglass specimens. Maximum and minimum width were chosen with the aim to maximize the radius of the waisted part as the greater the radius the smaller the stress concentration. First the two widths were taken equal to 19.0 mm and 12.7 mm as in the standardized bog-bone. The ratio between these widths is close enough to the desired one of 2/3 and the curvature radius of the waisted part in a sample with these widths would be of almost 234 mm. To increase the radius it was chosen to fix the two widths to 15 mm and 10 mm. The ratio between the two still respects the imposed one and the radius of the waisted part is almost 268 mm, generating a smaller stress concentration. The hourglass specimen obtained is depicted in Fig. 5b. The hourglass geometry described in paragraph 3 was adapted for the four-point bending test by increasing the length of the coupon extremities but without modifying the dimensions of the waisted central part, this way the total length of the coupon reached 130 mm as depicted in Fig. 6.

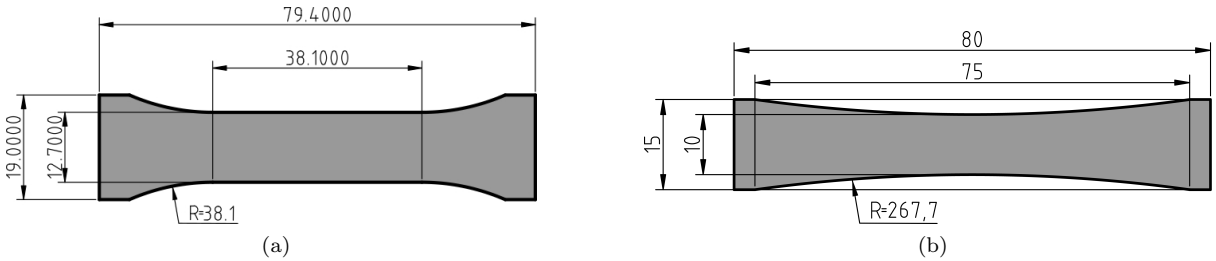

Figure 5: Flat specimen geometries used for pure compression test: a) dog-bone shaped ASTM-D695 specimen [20] ; b) new flat hourglass shaped specimen (dimensions are in mm) [21]

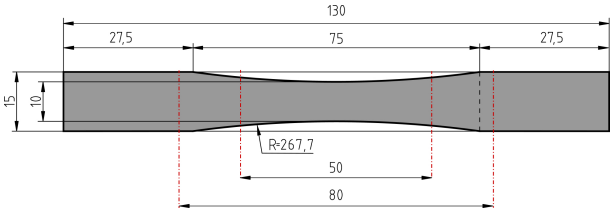

Figure 6: Flat Hourglass shaped specimen used for four-point bending tests (dimensions in mm) with initial cylinders contact position (red dash-dotted lines)

4. Four-point bending tests

4.1. Numerical simulation of the hourglass specimen geometry in bending

A parametric study was conducted on FEM software ABAQUS with the aim to find the right dimensions for the loading and supporting spans and the thickness of the coupon. The simulation model is depicted in Fig. 7. The fixture was simulated as four half cylinders (support and loading rollers) to reduce computational time. The four entities were defined as solids meshed with R3D4 elements. The support rollers were completely fixed. A downward displacement was imposed on the loading rollers and rotations were blocked. Taking advantage of symmetry, only half coupon was simulated as a 2D shell entities meshed with S3 elements. The thickness of the specimen has been taken into account in the definition of the contact points. Contacts between specimen and rollers were defined as frictionless to ease the simulation. Not having yet completed compression characterization, the material was simulated as linear elastic with the mechanical constants reported in Table 1. FEM convergence has been evaluated. S3 elements with a size of 0.6 mm and R3D4 elements with a size of 0.5 mm gave satisfactory results.

Due to limitations imposed by the fixture, the simulations were carried out until one of two conditions occurred:

1. load exceed 800 N (maximum applicable load of the fixture);

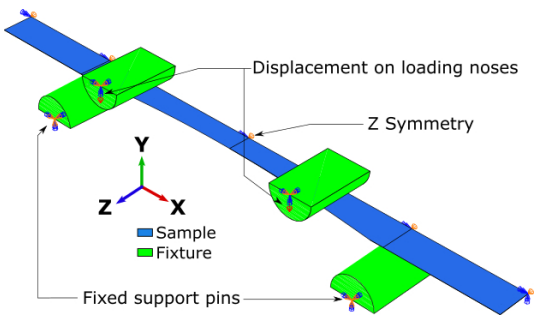

Figure 7: Four-point bending simulation model scheme

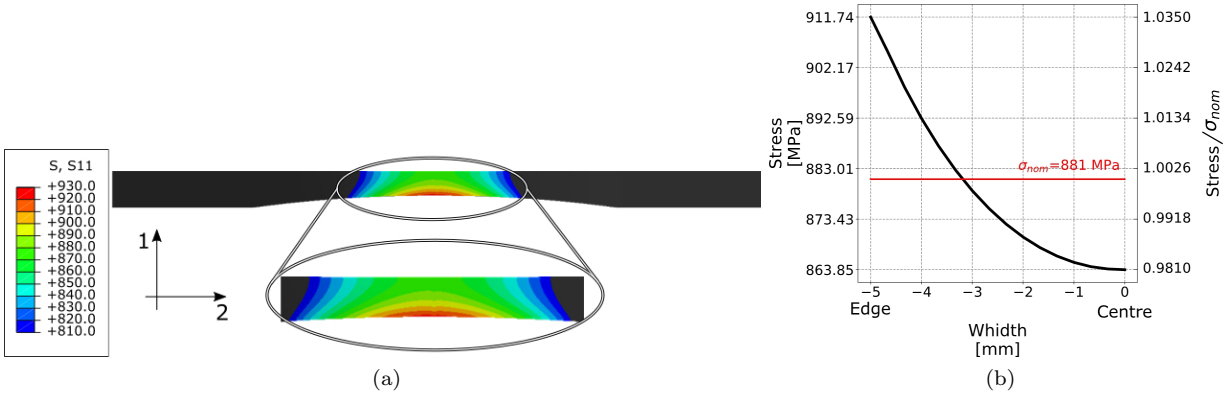

(a) (b)

Figure 8: Four-point bending test simulation: a) stress field on the face in tension of the flat hourglass shaped specimen for a nominal stress of 881 MPa [21]; b) stress distribution generated by the hourglass shape at the centre of the specimen on the face in tension

2. maximum specimen's deflection exceed 20 mm.

The two conditions were necessary as once one of the two was met during testing, the fixture's support rollers slipped out of their grooves, invalidating the final part of the test. Finally, the result of the simulation was considered valid if the average longitudinal stress in the elements at the centre of the specimen exceeded 800 MPa, meaning approximatively specimen failure. To limit deflection and applied load, the loading span was fixed at 50 mm and the support span at 80 mm.

Simulations were performed to find the optimal thickness of the coupon respecting the constraints dictated by the fixture. Finally a $[0]_{14}$ layup was choose as it failed for a load of 600 N (Fig. 9a), thicker laminates broke for loads greater than the limit of the fixture while, thinner laminate yielded an excessive deflection.

Fig. 8a depicts the longitudinal stress field in the out-most ply in tension. Even if the radius is smaller with respect to the 1002 mm of the tension specimen, simulation shows how the chosen hourglass shape helps at maintaining a homogeneous stress field in the central area of the specimen. The in-plane stress concentration coefficient of this coupon in bending, $S_{hourglass\_B}$, is estimated to a value of 1.035 as depicted in Fig. 8b. It should be noted that the stress gradient near the edge of the coupon (Fig. 8b) should not be confused with the through-thickness gradient studied by Wisnom *et al.* in [7–9, 22] necessarily present in bending and much higher.

Simulations were also carried out to verify that parasite mid-span beam axial force were not generated by the fixture due to large displacements and rotations. If present, this force would subject the specimen to a mix of compression or tension and bending making more difficult behaviour identification. By comparing the strains on the two surfaces, no significant difference was found, meaning that no parasite longitudinal loading is generated which signify that, under ideal conditions, the specimen is loaded in pure bending.

4.2. Evaluation of hourglass specimen and methodology on an E-Glass/epoxy composite

Four-point bending tests were conducted on a MTS1000 universal testing machine using a fixture conforming to ASTM-D6272 on the specimen defined above (Fig. 6). Strain measurement was performed via 2D digital image correlation (DIC) using ARAMIS software and strain gauges were used to validate DIC measures.

The moment applied to the specimen was estimated with the geometrical procedure described in appendix to this article starting from the machine load and displacement without the need for a complex FEM analysis. The result of this geometrical procedure, using only the displacement and the force recorded from the machine, leads to a non-linear law linking applied load and imposed moment (solid black line in Fig. 9a). This curve can be compared to the results of the FEM simulation (dash-dotted black line). They are in very

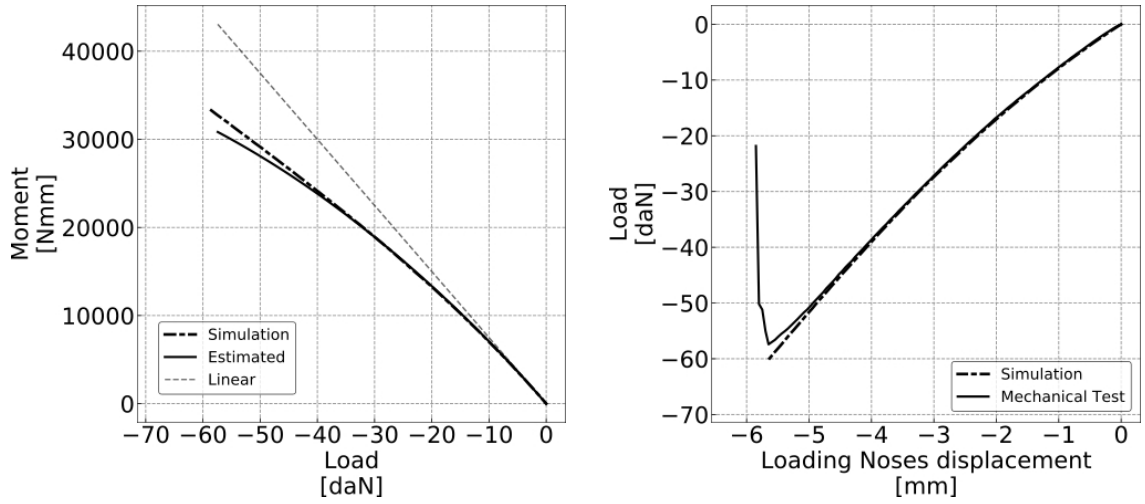

(a) (b)

Figure 9: Four-point bending test: comparison between an E-glass/epoxy specimen experimental test and FEM simulation: a) bending moment versus machine applied load ; b) machine applied load versus loading rollers displacement

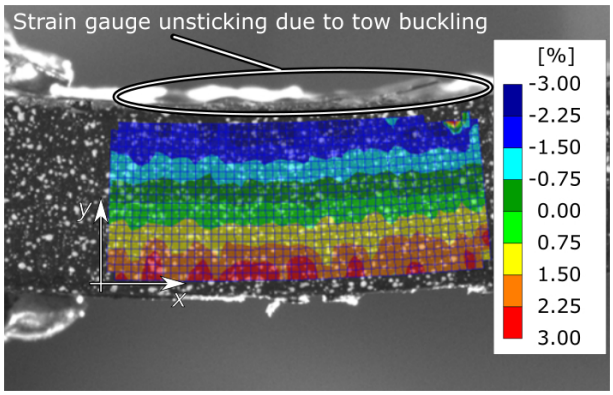

Figure 10: Four-point bending test: strain field measured with DIC on E-glass/Epoxy specimen side just before collapse [21]

good agreement except for the final part where damage starts to develop in the specimen. The figure shows also a large difference between a linear computation of the moment (grey dotted line) and a more realistic one. This discrepancy is also noticeable in the load versus displacement plot (Fig. 9b) where simulation and test result are in very good agreement. In conclusion, this comparison confirms previous assumptions and the approach proposed to compute bending moment.

Strains were measured via 2D DIC on one side of the specimens, on a 10×4.6 mm^2 surface located in the central part (Fig. 10). The camera used was equipped with a CCD chip with a resolution of 2448×2050 pixel^2 and an objective with a focal length of 50 mm. The camera was positioned 0.60 m away from the specimen. The acquisition was set to 20 pictures per millimetre of displacement with an exposure time between 40 ms and 65 ms depending on the speckles pattern on the coupons and an aperture of $f/8$. DIC generates a 2D mesh on the specimen surface (visible in Fig.10) and computes the strains in its nodes. Strain values were averaged lengthwise on the rows of the mesh to obtain their thickness-wise distribution:

$$\varepsilon^{avg}(y) = \frac{1}{N_{nodes}} \sum_{i=1}^{N_{nodes}} \varepsilon(x_i, y) \tag{2}$$

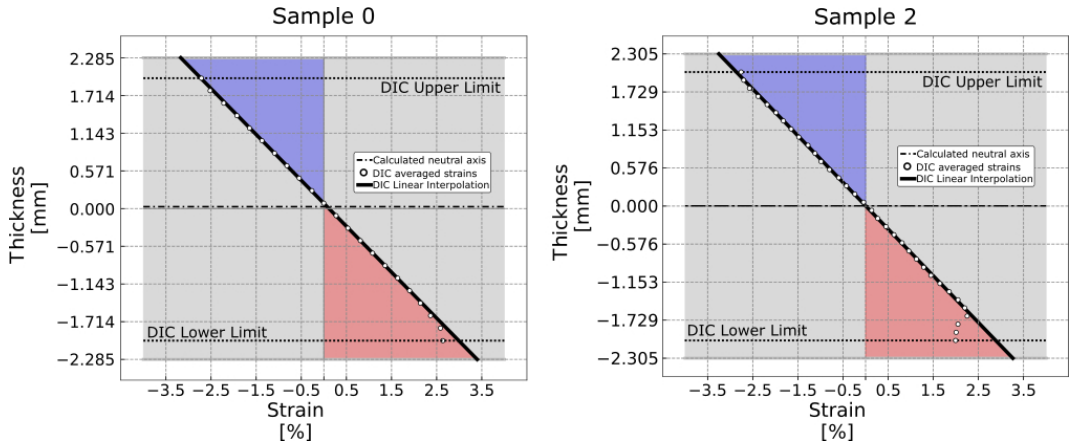

Figure 11: Four-point bending test: interpolated strain fields for E-Glass/epoxy specimens 0 and 2 just before collapse

Fig. 11 shows strains estimated after this averaging method for two example of specimens just before collapse (white points). In accordance to Kirchhoff hypothesis, strains are linear along the thickness. These measures show the absence of inter-ply delamination due to the continuity of the deformation and lack of 3D effects on the free edge. This permits to estimate strains on top and bottom surfaces via linear extrapolation from values obtained in the central part of the specimen (black line on Fig. 11). Maximum strains in tension and compression are very close. As a consequence, the computed neutral axis (dash-dotted line) is close to specimen's mid-plane even in the final stages of the test. This symmetric distribution of the strains implies that compression and tensile modulus are similar up to failure but not necessarily linear. For the case of the E-glass/Epoxy studied here, material behaviour in tension was demonstrated as slightly non-linear (Fig. 3a) due to the presence of irreversible transverse damage in the 17% of weft fibres. To justify the symmetric strain distribution, compressive behaviour must also be slightly non-linear, in this case a fibre non-linearity. Here we will neglect the slight non-linearity and approximate the material constitutive law as linear with compression and tensile modulus equivalent and constant up to failure:

$$\sigma(y) = E\varepsilon^{avg}(y) \tag{3}$$

The assumption of linear behaviour leads to a great simplification in the estimation of maximum stresses in the out-most plies applying Classical Beam Theory:

$$\sigma_{max} = \frac{M_f}{I}\,\frac{t}{2} = \frac{6M_f}{wt^2} \tag{4}$$

where I is the area moment of inertia of the specimen at the minimum width. This classical results gives also directly the Young's modulus with the relation $E = 6M_f/(\varepsilon_{max} w t^2)$.

Skin stress-strain plot of the three tests are depicted in Fig. 12 using Eqs. 2 and 4 under the assumption of linear behaviour, this assumption appears to be valid up to a deformation of 2%. Stress failure values are reported in Table 2. All specimens have broken in the central part of the face in tension without any visible delamination phenomena. The only compression linked phenomenon that we were able to notice was localized buckling of woven tows in correspondence of the interlocks where tow curvature is maximum (see Fig. 10). This phenomenon was limited to the tows, the rest of the surface did not present any sign of compression failure or surface buckling. This localized buckling leads to the unsticking of the strain gauges. As we can see on Fig. 12, strain values from DIC and gauges are very close except for the final part of the compression curves. Unsticking of the strain gauges explains these large discrepancies. This comparison validates the strain estimation protocol via DIC and shows the advantage of this method here.

Finally, the measured values for the average ultimate tensile stress, the ultimate tensile strain and the Young's modulus are equal to 881 ± 5.51 MPa, 3.28 ± 0.09% and 29 ± 0.7 MPa, respectively. Higher values of

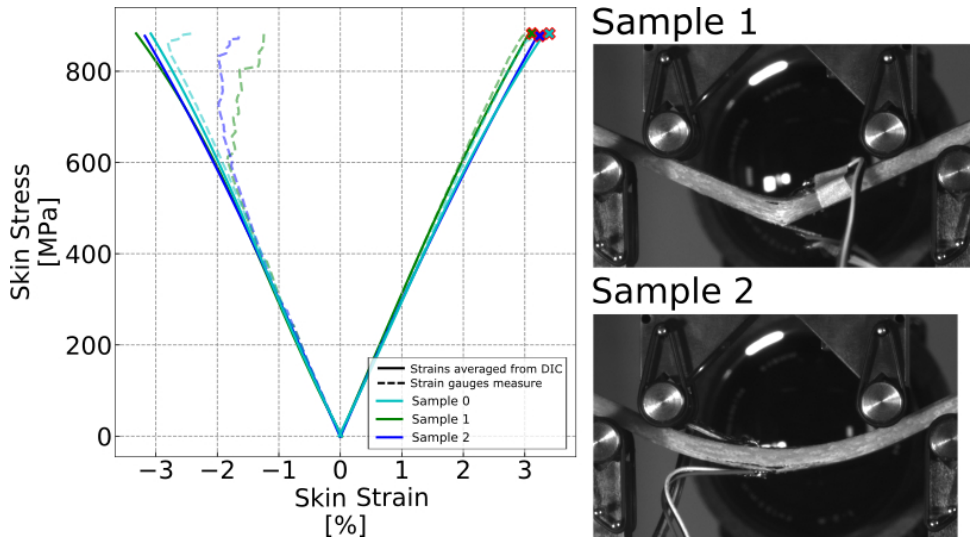

Figure 12: Four-point bending test: skin stress/strain results for three different E-glass/Epoxy specimens (cross = failure) and picture of the specimens just after collapse

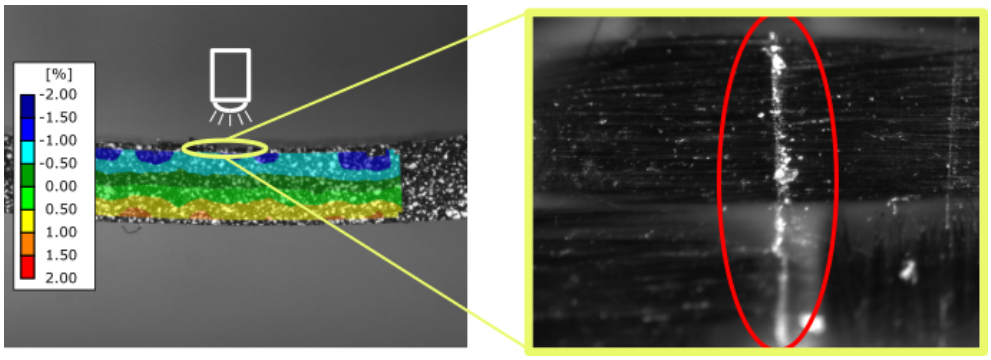

Figure 13: Four-point bending test: strain field measured with DIC on Carbon/PEEK specimen side just before collapse and out-of-plane kink-band failure (at right).

tensile strain at failure are observed in bending tests in comparison with tensile tests (Tab. 2). This result on the ultimate tensile strain has also been found by Wisnom and Atkinson in four-point bending tests in [15]. These authors linked this phenomena to the size effect studying specimens of different thicknesses. This effect can be also observed in the presence of in-plane stress gradients generated by a stress concentration (plate with a hole, a notch, etc.) where strains much higher than tensile failure strain are recorded before failure [23]. It should be noted that, for the thickness tested here, E-glass/epoxy coupons always failed in tension. In conclusion, the hourglass shape assures to obtain failure at the centre of the specimen in four-point bending.

4.3. Evaluation of hourglass specimen and methodology on a carbon/PEEK composite

To complete the analysis of the optimized flat hourglass geometry, the same testing protocol was applied to a carbon/PEEK 5-harness satin weave 3K woven composite (T300J, PiPreg 3106-1250P0378). Only one hourglass specimen with the same dimensions depicted in Fig. 6 was tested. The specimen failed again in the centre but, in this case, on the compression side. Test was stopped as soon as kink-bands appeared on the surface of the specimen. Fig. 13 depicts the strain field and local out-of-plane fibre buckling on the surface similar to that observed by Soutis and Turkmen [24].

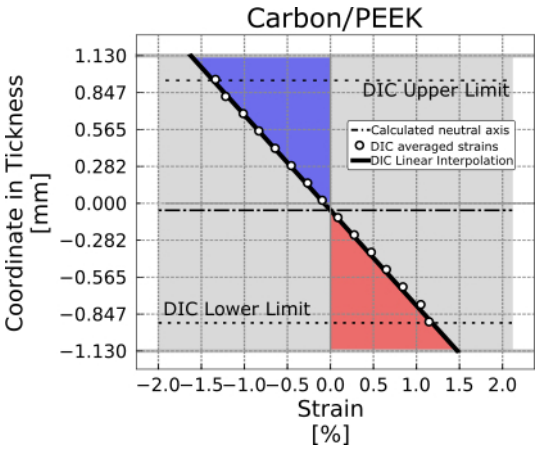

Figure 14: Four-point bending test: interpolated strain fields for Carbon/PEEK specimen just before collapse

Fig. 14 shows strain distribution for the Carbon/PEEK specimen. Material behaviour is non-linear as extremal strains sensibly differ (approximately, 1.45 % and -1.6 % on the figure) [25, 26], the bending neutral axis is shifted towards the tensile part implying a tangential compressive modulus inferior to Young's Modulus, consequentially the estimation of the material behaviour is complicated by this non-linearity and a different procedure has to be used to analyse the results of the test. To estimate the stress-strain curve, the power-law model already proposed by Allix [27] is used, as in [28], for the compressive constitutive law:

$$\sigma = (1 + \beta\,\varepsilon^{\gamma})\,E\,\varepsilon \tag{5}$$

where E is the Young's modulus identified in tension (see. 2).

This permits to identify only the non-linearity parameters γ and β for the compressive constitutive law (Eq. 5). Using the error minimization procedure proposed in [28], γ was found near a value of 1 because the non-linearity is relatively low. Consequentially, γ was fixed to 1 and β was found equal to 17. The result of the identified constitutive law fits well the experimental data as represented in Fig. 15 where equivalent stress is computed with Eq. 4. Compressive failure occurred for a stress of 730 MPa and a strain of -1.6 %.

In bending, coupons are subjected to a through thickness strain gradient in the failure zone. As found in literature, the effect of this gradient is to generate higher compressive failure strains compared to the ones measured in its absence [8, 9, 22].

In conclusion, for the carbon/PEEK composite, the hourglass-shaped specimen still permits to avoid failure far from the load introduction points. However, the effect of the strain gradient in thickness does not make possible to directly estimate the material strength. Moreover, the behaviour determination, when non-linear, demands a more complex calculation procedure when compared to a pure compression test as the one studied in the second part of the article.

5. Compressive tests

5.1. Definition of hourglass specimen and testing procedure

Compressive tests were performed on a 3R Syntax 100 with the help of an anti-buckling fixture conform to ASTM D695 [20]. Both dog-bone shaped ASTM D695 and new flat hourglass shaped specimens were tested using this fixture thanks to the same height and thickness, and close width (Fig. 5). The dog-bone and hourglass shapes utilized for the specimens are depicted in Fig. 5. In the case of the adapted hourglass shape the stress concentration factor in compression is calculated from a FEM simulation as the ratio between the nominal stress imposed to the specimen and the highest stress recorded along its centre. This yielded a value of $S_{hourglass\_C} = 1.045$.

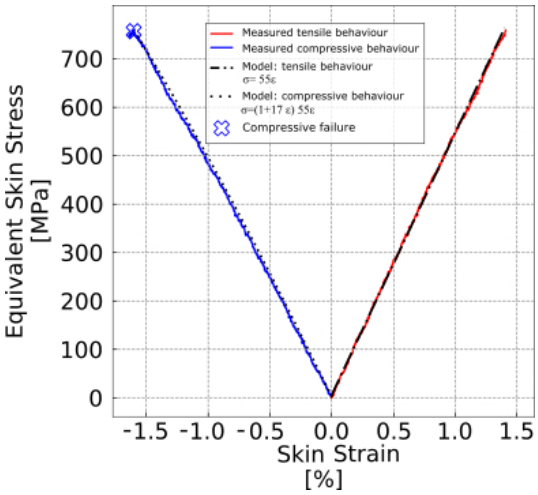

Figure 15: Four-point bending test: skin strain/stress results for a Carbon/PEEK specimen (cross = failure)

Before testing, particular attention was put in the preparation of the coupons, parallelism of the upper and lower faces is mandatory to avoid coupon misalignment and consequent premature ends failure. Specimens were positioned between the anti-buckling surfaces of the fixture, afterwards the retaining screws were finger tightened. The screws were not over-tightened to avoid specimen jamming under load and introduction of a compression force in thickness direction. Longitudinal strains were measured for both specimen types using a video-extensometer from Limess on the side of the coupons and video-extensometer images were also treated with 2D DIC (Fig. 16). Video-extensometer requires two line markers with good contrast. Black-white stickers were used with a calibrated distance of 20 mm for this reason.

5.2. Evaluation of hourglass specimen and methodology on an E-Glass/epoxy composite

First of all, the measurement obtained from the video-extensometer was compared to the measure from DIC in the same region of interest (ROI). For the dog-bone shaped specimens, the ROI is flat and strain measured via DIC varied in a range between -2.2% and -2.6% (Fig. 17) possibly due to heterogeneities in the material and errors in the measurement technique. However, the averaged DIC and the video-extensometer resulted in the same values. For the hourglass specimens, the ROI is curved (highlighted in red in Fig. 18). DIC measurements in the ROI varied between -2.5% and -2.9% with the same variation as the values obtained for the dog-bone coupon. Consequentially we can consider that the strain field is homogeneous in the waisted part. As with the dog-bone coupon the averaged DIC strain and the video-extensometer yielded the same values (black and red lines in Fig. 18).

Seven standard dog-bone shaped and three hourglass shaped E-Glass/epoxy specimens were tested. Only three hourglass specimens were tested because, due to manufacturing problems (poor quality of the end surfaces), other specimens were deemed not suitable for testing. Dog-bone specimens failed for a stress level of 688 ± 18 MPa with an average longitudinal strain at failure of $-2.24 \pm 0.08\%$ (Fig. 19). Full results are reported in Table 2. As usual, it can be noted in the table that the coefficient of variation (COV) is larger in compression (around 3%) than in bending or in tension (around 1%). Experimental curves confirmed behaviour linearity in compression up to a strain of 2%. Failure occurred systematically in the upper tapered part, in proximity of the loaded end. This failure position can be explained by the presence of friction between specimen and fixture and will be discussed in the next paragraph. The three hourglass shaped specimens failed in the central part of the coupon but not in the middle where highest compression stresses should be present. The average ultimate stress at failure was equal to 765 ± 23 MPa and average longitudinal strain at failure was equal to -2.72 ± 0.04 % (Fig. 19). This ultimate strain at failure is close to the values obtained by Kim and Crasto [29] on E-Glass/Epoxy fabric using original miniature sandwich specimens, more complex to manufacture. Looking only at failure stresses, the use of the hourglass geometry

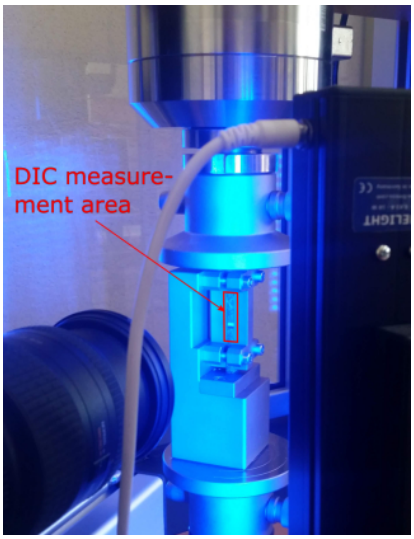

Figure 16: Pure compression test: specimen DIC measurement area (after failure, only one Black-white sticker is visible)

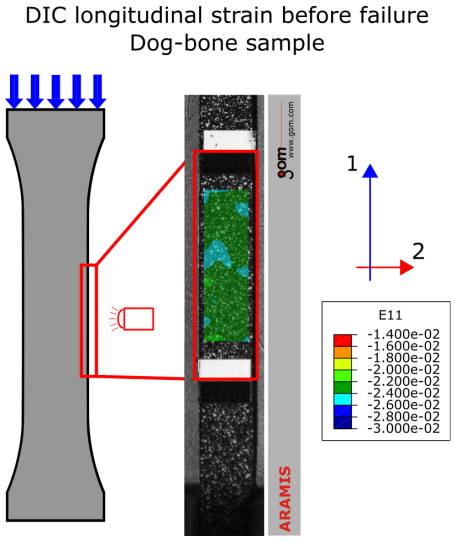

Figure 17: Pure compression test: longitudinal strain fields of E-Glass/Epoxy dog-bone specimen before failure measured via DIC

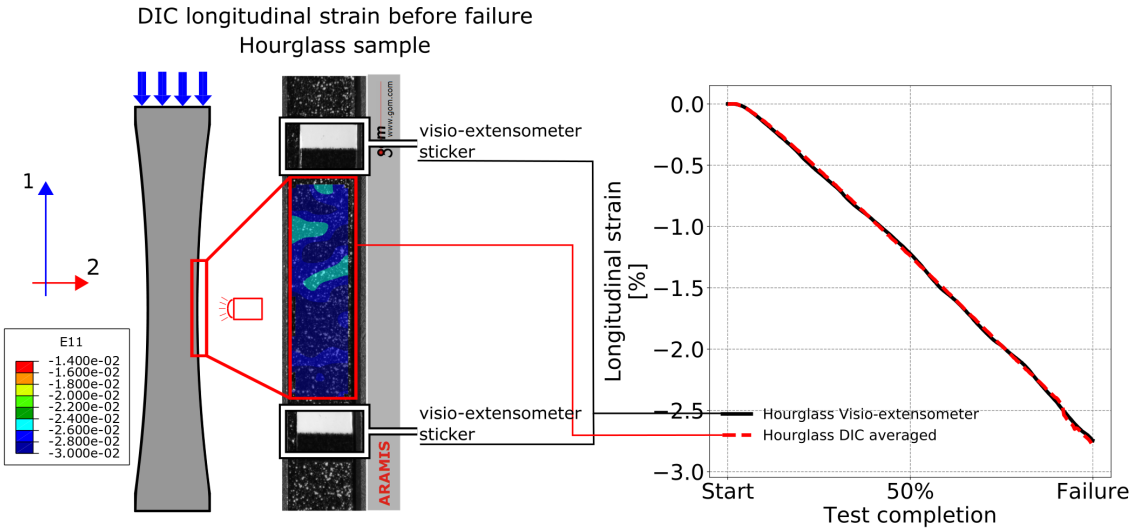

Figure 18: Pure compression test: longitudinal strain fields of E-Glass/Epoxy hourglass specimen before failure measured via DIC

lead to a gain of 11% compared to the dog-bone, avoiding failure in a zone characterized by a sharp width variation and large stress concentration. The adoption of the hourglass shape lead to an even greater increase of failure strain with a gain of 24% due to the non-linearity of the material.

To understand the influence of specimen geometry and why failure occurred systematically in proximity of the loaded side, qualitative FEM simulations taking into account friction, were conducted on ABAQUS software (Fig. 20). The specimens were simulated as 3D deformable solids with C3D6 and C3D4 elements to take into account out of plane effects (e.g. Poisson's effect and out-of-plane compression), minimum element size in contact zones was 0.5 mm to limit simulation time. Engineering constants of the material are reported in Table 1. Constants in out-of plane direction were supposed equal to constants in transverse direction due to the quasi-unidirectional nature of the Glass/Epoxy woven. For the fixture, only the two surfaces in contact with the specimen (anti-buckling grooves) were simulated as fixed rigid surfaces. Therefore, deformation of the anti-buckling fixture (guides, screws, etc.) is not considered. Contact with friction is considered with a friction coefficient of 0.3. Specimens were fixed on one end and on the other a compression load was imposed. Simulations were stopped as the mechanical test failure load was reached, no failure criteria were implemented. As the compression load increases, the friction effect is more and more important due to the Poisson's effect in the thickness. Simulated strain fields were superimposed over images of broken specimens in Fig. 21. Results of the simulations are very different for both specimens showing the interest of the new specimen geometry. From the images of the dog-bone specimen (Fig. 21a), it appears clearly that failure initiates from a zone where a sharp longitudinal stress gradient is present independently of the friction coefficient, in absence of friction the stress concentration coefficient ($S_{dogbone\_C}$) in this zone was estimated equal to 1.20 by FEM simulation. In the case of the hourglass shape specimen (Fig. 21b) the stress concentration coefficient ($S_{hourglass\_C}$) of the sample yielded a value of 1.045. The 3D simulations showed how the zone with the maximum longitudinal stress shifts towards the loaded end if friction is considered. For the hourglass coupon, failure position does not correspond with the maximum simulated stress due to the complexity of the problem and the qualitative nature of our FEM simulation (unknown friction coefficient).

In conclusion, the hourglass-shaped specimen geometry gives satisfactory results in compression for this kind of material even if the failure happen in the central part of the specimen but not in the middle. This last point can be explained by the combined effect of material Poisson ratio and friction in the anti-buckling system.

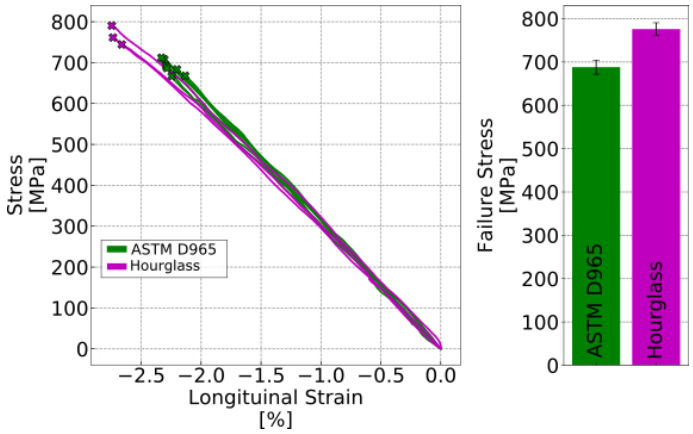

Figure 19: Pure compression test: stress-strain curves and mean stress at failure for both E-Glass/Epoxy specimen geometries [21]

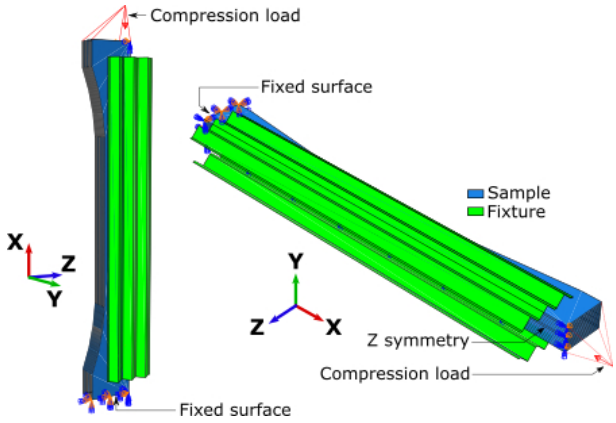

Figure 20: Pure compression test: FEM simulation model scheme for ASTM D695 fixture in ABAQUS

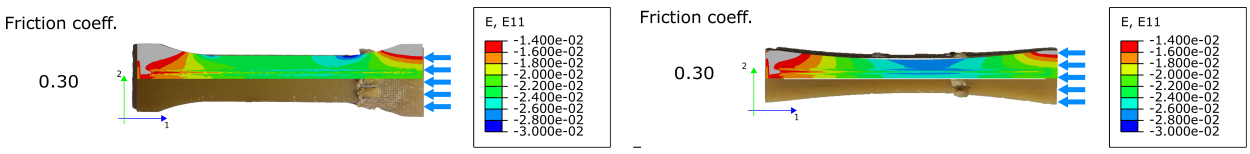

(a) (b)

Figure 21: Pure compression test: FEM simulations superimposed over E-Glass/Epoxy failed specimens: a) ASTM D695 dog-bone shaped specimens , b) flat hourglass shaped specimens

Testing method	Layup	Specimen	S_{coupon}	Failure position	Failure stress/Failure strain									
					C1	C2	C3	C4	C5	C6	C7	Av.	StD	COV
					MPa/%									%
Tensile	$[0°]_8$	Hourglass	1.029	Specimen centre	756	745						750	8	1.0
					2.618	2.560						2.59	0.03	1.16
Four-points bending	$[0°]_{16}$	Hourglass	1.035	Specimen centre	884	875	885					881	5.5	0.6
				on tension surface	3.19	3.26	3.40					3.28	0.09	2.74
Compressive ASTM D-695	$[0°]_{16}$	Dog-bone	1.20	Close to sharp	708	712	684	692	668	667	687	688	18	2.6
				width variation	-2.31	-2.33	-2.29	-2.29	-2.13	-2.25	-2.11	-2.24	0.09	4.01
		Hourglass	1.045	Close to	790	761	744					765	23	3.0
				specimen's centre	-2.75	-2.74	-2.66					-2.72	0.04	1.47

Table 2: Testing results on various configurations of E-Glass/epoxy (M42ST/1055) (S_{coupon} = stress concentration coefficient; C = coupon; Av.= average; StD = standard deviation; COV = coefficient of variation)

6. Conclusion

In this paper we have proposed the use of an hourglass shaped specimen to study compression behaviour of FRP in four-point bending and compression tests. As previously shown in tensile testing [12, 13], this particular shape, ensures failure at the centre of the coupon in a zone where the stress field is subjected to a negligible in-plane gradient, avoiding failure due to stress concentrations. Dimensions of the specimens were adapted for four-point bending test and end compression test. This geometry generated only a slight in-plane stress gradient in the central part of the specimen in both bending and compression, resulting in stress concentration coefficients of 1.035 and 1.045 respectively. In four-point bending, failure always occurred at the centre of the hourglass coupons.

The short hourglass shape specimen was compared to a standardized dog-bone specimen in pure compression tests on an end-compression fixture conform to ASTM D-695. Hourglass specimens performed better than the standardized dog-bone as stress and strain at failure were higher. Failure position was also different, dog-bone specimens failed in a zone characterized by a sharp width variation far from the centre. Hourglass specimens failed close to the centre. FEM simulations of the ASTM D695 test demonstrated how the dog-bone shape generates the strongest stress concentration causing premature failure of the specimens. The use of the hourglass coupons permitted to identify the constitutive equation of the material.

Both four-point bending and ASTM D-695 compression testing techniques present advantages and drawbacks. The ASTM D-695 compression test is simple to analyse, it gives direct access to the constitutive equation of the material and permits to get closer to the pure compressive resistance when using the anti-buckling fixture together with the hourglass shaped coupons. Four point bending permits to avoid buckling in compression. The determination of behaviour laws is complicated by the necessity to estimate the bending moment in presence of large displacements and rotations. To accomplish this task a geometrical protocol is proposed and validated against FEM simulations. Other factors that complicate the procedure are non-linearities of the material, while ultimate strength determination is not directly possible due to the presence of the strain gradient through the thickness as reported by Wisnom *et al.* [7–9, 22].

Acknowledgements

This research is financially supported by the French Ministry of the Armed Forces through the Directorate General of Armaments.

Appendix: Bending moment calculation method

As demonstrated by Mujika [30, 31], the main sources of error in estimation of mechanical properties from four-point bending tests are the contact points between specimen and fixture. During a test, position of

Parameter	Notation	Unit	Value
Minimum width of the specimen	w	mm	10
Thickness of the specimen	t	mm	2.64
Rollers radius	r	mm	5
Loading roller (L) centre	(x_{cL}, y_{cL})	mm	n/a
Supporting roller (S) centre	(x_{cS}, y_{cS})	mm	n/a
Loading roller contact point coordinates	$(x_{contact\,L}, y_{contact\,L})$	mm	n/a
Supporting roller contact point coordinates	$(x_{contact\,S}, y_{contact\,S})$	mm	n/a
specimen's slope	m_{tg}	-	n/a

Table 3: Four-point bending test: geometrical notations (n/a = not applicable)

contact points constantly changes, consequentially magnitude of imposed moment is not directly proportional to applied load. This means that a correction must be applied to estimate the real magnitude of the moment. A procedure is proposed here to compute this correction (Fig. 22a).

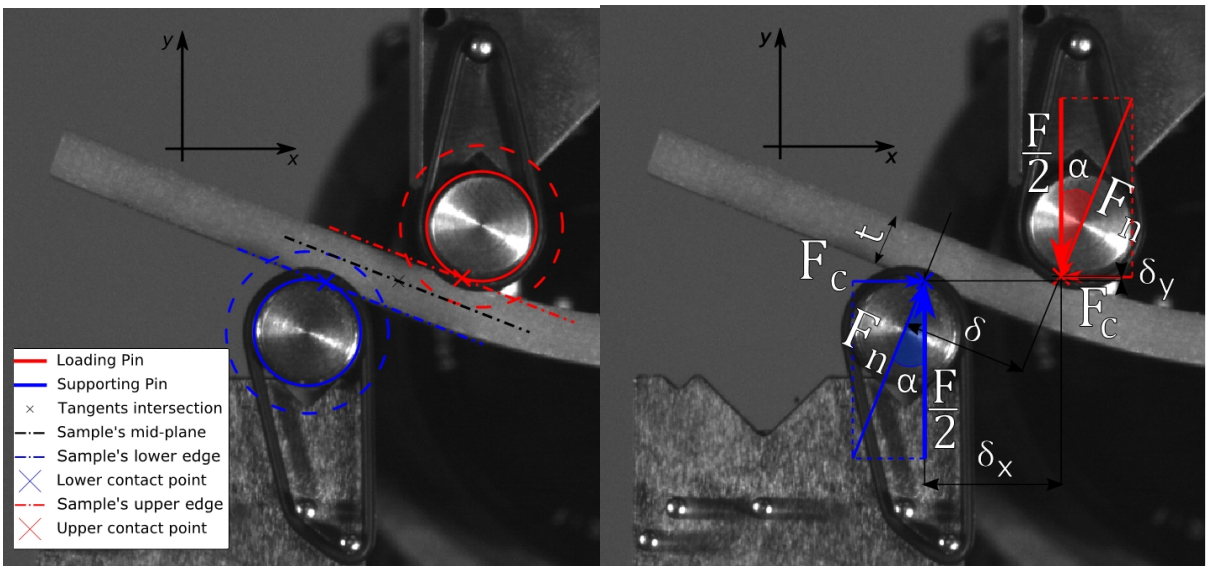

(a) (b)

Figure 22: Four-point bending test: a) span estimation procedure ; b) forces decomposition for moment estimation

Focusing on one side of the fixture, vertical position of loading roller is always known from machine's displacement and can be utilized to estimate the position of the contact points. We can assume that the coupon remains always straight between the supporting roller and the loading roller (this assumption is confirmed during testing as shown in Fig. 22b) and always touches both. Under these assumptions, the specimen can be represented by a straight line (representing his mid plane) tangent to two circumferences of radius equal to that of the rollers plus half of the specimen's thickness (dashed circles in Fig. 22a). The known parameters of the geometry are given in Table 3. Geometrically, two incident lines are tangent to two circles and they intersect in a point P_{int} of coordinates (x_{Pint},y_{Pint}) (black cross in Fig. 22a) given by the following equation:

$$\begin{cases} x_{Pint} &= \frac{1}{2}(x_{cL} + x_{cS}) \\ y_{Pint} &= \frac{1}{2}(y_{cL} + y_{cS}) \end{cases} \tag{6}$$

One of these lines represents the mid-plane of the specimen (black dash-dotted line in Fig. 22a). Its slope (m_{tg}) can be computed via the coordinates of its two tangent points (blue crosses in Fig. 22a):

$$m_{tg} = \frac{y_{PtgL} - y_{PtgS}}{x_{PtgL} - x_{PtgS}} \tag{7}$$

where coordinates of these tangent points are given using the following equations:

$$\begin{aligned} x_{Ptg\,k} &= x_{c\,k} + \frac{r^{*2}(x_{Pint} - x_{c\,k})}{(x_{Pint} - x_{c\,k})^2 + (y_{Pint} - y_{c\,k})^2} \\ &+ \frac{-r^*(y_{Pint} - y_{c\,k})\sqrt{(x_{Pint} - x_{c\,k})^2 + (y_{Pint} - y_{c\,k})^2 - r^{*2}}}{(x_{Pint} - x_{c\,k})^2 + (y_{Pint} - y_{c\,k})^2} \qquad \text{for} \quad k \in \{L, S\} \end{aligned} \tag{8}$$

$$\begin{aligned} y_{Ptg\,k} &= y_{c\,k} + \frac{r^{*2}(y_{Pint} - y_{c\,k})}{(x_{Pint} - x_{c\,k})^2 + (y_{Pint} - y_{c\,k})^2} \\ &+ \frac{r^*(x_{Pint} - x_{c\,k})\sqrt{(x_{Pint} - x_{c\,k})^2 + (y_{Pint} - y_{c\,k})^2 - r^{*2}}}{(x_{Pint} - x_{c\,k})^2 + (y_{Pint} - y_{c\,k})^2} \qquad \text{for} \quad k \in \{L, S\} \end{aligned} \tag{9}$$

with $r^* = r + t/2$. This way, the specimen's angle respect to the horizontal is linked to its slope by: $\alpha = \tan^{-1}(m_{tg})$.

Under the hypothesis that specimen is always straight between the two rollers we can assume that the slope of its edges (green and red dash-dotted lines in Fig. 22a) is the same as its mid-plane (m_{tg}). Intercepts of the two lines representing the edges of the specimen are found by solving the two systems given by the equation of the lines and the equations of the two circles representing the rollers (solid lines in Fig. 22a) and imposing tangency between the two entities. The searched intercepts quantities q_L and q_S, for the lower and upper edge respectively, are given by:

$$\begin{cases} q_L &= -m_{tg}x_{c\,L} + r\sqrt{m_{tg}^2 + 1} + y_{c\,L} \\ q_S &= -m_{tg}x_{c\,S} - r\sqrt{m_{tg}^2 + 1} + y_{c\,S} \end{cases} \tag{10}$$

Once all parameters describing the lines are known, the same systems can be solved for x and y to find the coordinates of the tangent points representing the contact points between the specimen and the rollers (green and red crosses in Fig. 22a):

$$x_{contact\,k} = -\frac{m_{tg}q_k - x_{c\,k} - m_{tg}y_{c\,k}}{m_{tg}^2 + 1} \qquad \text{for} \quad k \in \{L, S\} \tag{11}$$

$$y_{contact\,k} = m_{tg}x_{contact\,k} + q_k \qquad \text{for} \quad k \in \{L, S\} \tag{12}$$

Their horizontal span (δ_x) and vertical span (δ_y) are respectively equal to:

$$\delta_x = x_{contact\,S} - x_{contact\,L} \tag{13}$$

$$\delta_y = y_{contact\,S} - y_{contact\,L} \tag{14}$$

Neglecting friction, the effort normal to the neutral axis of the specimen F_n, can be decomposed in a vertical force equal to half the machine applied load (F), and a horizontal force F_c:

$$\frac{F}{2} = F_n\,\cos(\alpha) \tag{15}$$

$$F_c = F_n \sin(\alpha) \tag{16}$$

The span (δ) between the two $F_n$is equal to:

$$\delta = \delta_x \cos(\alpha) - \delta \sin(\alpha) \tag{17}$$

The second member of Eq. 17 is negligible when compared to the first as the vertical span $\delta_y$is negligible compared to δ_x.

Finally, pure bending moment is calculated:

$$M_f = -F_n \delta = -\frac{\delta_x F}{2} + F_c \delta_y = \frac{F}{2}(\delta_y \tan(\alpha) - \delta_x) \tag{18}$$

This procedure permits to estimate the real bending moment during a four-point bending test only knowing the position of the loading rollers without the need to constantly track the position of the specimen.

References

[1] D. Woolstencroft, A. Curtis, R. Haresceugh, A comparison of test techniques used for the evaluation of the unidirectional compressive strength of carbon fibre-reinforced plastic, Composites 12 (4) (1981) 275–280. doi:10.1016/0010-4361(81)90018-5.
URL http://linkinghub.elsevier.com/retrieve/pii/0010436181900185

[2] J. Harper, N. Miller, S. Yap, Problems associated with the compression testing of fibre reinforced plastic composites, Polymer Testing 12 (1) (1993) 15–29. doi:10.1016/0142-9418(93)90023-I.
URL http://linkinghub.elsevier.com/retrieve/pii/014294189390023I

[3] K. Schneider, Determination of Compressive Properties of Fibre Composites in the In-plane Direction According to ISO 14126. Part 1: A Round Robin Test, Applied Composite Materials 14 (1) (2007) 1–15. doi:10.1007/s10443-006-9027-6.
URL http://link.springer.com/10.1007/s10443-006-9027-6

[4] T. A. Bogetti, J. W. Gillespie, R. B. Pipes, Evaluation of the IITRI Compression Test Method for Stiffness and Strength Determination, Composites Science and Technology 32 (1) (1998) 57–76.

[5] S. C. Tan, Stress analysis and the testing of celanese and iitri compression specimens, Composites science and technology 44 (1) (1992) 57–70.

[6] W. C. Cui, M. R. Wisnom, Contact finite element analysis of three-and four-point short-beam bending of unidirectional composites, Composites science and technology 45 (4) (1992) 323–334.

[7] M. Wisnom, The effect of specimen size on the bending strength of unidirectional carbon fibre-epoxy, Composite Structures 18 (1) (1991) 47–63.

[8] M. Wisnom, J. Atkinson, Constrained buckling tests show increasing compressive strain to failure with increasing strain gradient, Composites Part A: Applied Science and Manufacturing 28 (11) (1997) 959–964. doi:10.1016/S1359-835X(97)00067-5.
URL http://linkinghub.elsevier.com/retrieve/pii/S1359835X97000675

[9] M. Wisnom, J. Atkinson, M. Jones, Reduction in compressive strain to failure with increasing specimen size in pin-ended buckling tests, Composites Science and Technology 57 (9-10) (1997) 1303–1308. doi:10.1016/S0266-3538(97)00057-2.
URL http://linkinghub.elsevier.com/retrieve/pii/S0266353897000572

[10] M. Arhant, P.-Y. Le Gac, M. Le Gall, C. Burtin, C. Briançon, P. Davies, Effect of sea water and humidity on the tensile and compressive properties of carbon-polyamide 6 laminates, Composites Part A: Applied Science and Manufacturing 91 (2016) 250–261.

[11] H. Fukuda, M. Itabashi, Simplified compression bending test method for advanced composites, Composites Part A: Applied Science and Manufacturing 30 (3) (1999) 249–256. doi:10.1016/S1359-835X(98)00160-2.
URL http://linkinghub.elsevier.com/retrieve/pii/S1359835X98001602

[12] I. De Baere, W. Van Paepegem, C. Hochard, J. Degrieck, On the tension-tension fatigue behaviour of a carbon reinforced thermoplastic part II: Evaluation of a dumbbell-shaped specimen, Polymer Testing 30 (6) (2011) 663–672. doi:10.1016/j.polymertesting.2011.05.005.
URL https://linkinghub.elsevier.com/retrieve/pii/S0142941811000791

[13] J. Payan, C. Hochard, Damage modelling of laminated carbon/epoxy composites under static and fatigue loadings, International Journal of Fatigue 24 (2-4) (2002) 299–306.

[14] B. Öztürk, P. Gromala, C. Silber, K. Jansen, L. Ernst, Finite element based design of a new dogbone specimen for low cycle fatigue testing of highly filled epoxy-based adhesives for automotive applications, in: 2013 14th International Conference on Thermal, Mechanical and Multi-Physics Simulation and Experiments in Microelectronics and Microsystems (EuroSimE), IEEE, 2013, pp. 1–4.

[15] M. Wisnom, J. Atkinson, Reduction in tensile and flexural strength of unidirectional glass fibre-epoxy with increasing specimen size, Composite Structures 38 (1-4) (1997) 405–411. doi:10.1016/S0263-8223(97)00075-5.
URL http://linkinghub.elsevier.com/retrieve/pii/S0263822397000755

[16] G. Eyer, O. Montagnier, J.-P. Charles, C. Hochard, Design of a composite tube to analyze the compressive behavior of CFRP, Composites Part A: Applied Science and Manufacturing 87 (2016) 115–122. doi:10.1016/j.compositesa.2016.04.006.
URL https://linkinghub.elsevier.com/retrieve/pii/S1359835X16300732

[17] G. Eyer, O. Montagnier, J.-P. Charles, C. Hochard, Effet de l'endommagement transverse sur la résistance en compression sens fibre d'un composite carbone/époxy (2013) 11.
[18] G. Eyer, Rupture des matériaux composites en compression sens fibre. Analyse de l'effet de l'endommagement., PHD Thesis, Université d'Aix-Marseille (Jul. 2015).
[19] C. Hochard, Y. Thollon, A generalized damage model for woven ply laminates under static and fatigue loading conditions, International Journal of Fatigue 32 (1) (2010) 158–165. doi:10.1016/j.ijfatigue.2009.02.016.
URL https://linkinghub.elsevier.com/retrieve/pii/S0142112309000619
[20] ASTM, Standard test method for compressive properties of rigid plastics (2015).
[21] A. Cocchi, C. Hochard, O. Montagnier, F. Mazerolle, Influence de l'endommagement matriciel sur la résistance en compression sens fibre pour des composites stratifiés, in: 2019 Journées Nationales sur les Composites (JNC21), Bordeaux, 2019.
[22] M. Wisnom, On the high compressive strains achieved in bending tests on unidirectional carbon-fibre/epoxy, Composites Science and Technology 43 (3) (1992) 229–235. doi:10.1016/0266-3538(92)90093-I.
URL http://linkinghub.elsevier.com/retrieve/pii/026635389290093I
[23] C. Hochard, N. Lahellec, C. Bordreuil, A ply scale non-local fibre rupture criterion for CFRP woven ply laminated structures, Composite Structures 80 (3) (2007) 321–326. doi:10.1016/j.compstruct.2006.05.021.
URL https://linkinghub.elsevier.com/retrieve/pii/S0263822306002285
[24] C. Soutis, D. Turkmen, Moisture and Temperature Effects of the Compressive Failure of CFRP Unidirectional Laminates., Journal of Composite Materials 31 (8) (1997) 832–849. doi:https://doi.org/10.1177/002199839703100805.
[25] R. M. Jones, Apparent Flexural Modulus and Strength of Multimodulus Materials, Journal of Composite Materials 10 (4) (1976) 342–354. doi:10.1177/002199837601000407.
URL http://journals.sagepub.com/doi/10.1177/002199837601000407
[26] F. Mujika, N. Carbajal, A. Arrese, I. Mondragon, Determination of tensile and compressive moduli by flexural tests, Polymer Testing 25 (6) (2006) 766–771. doi:10.1016/j.polymertesting.2006.05.003.
URL https://linkinghub.elsevier.com/retrieve/pii/S0142941806000948
[27] O. Allix, P. Ladevèze, E. Vittecoq, Modelling and identification of the mechanical behaviour of composite laminates in compression, Composites Science and Technology 51 (1) (1994) 35–42. doi:10.1016/0266-3538(94)90154-6.
URL https://linkinghub.elsevier.com/retrieve/pii/0266353894901546
[28] O. Montagnier, C. Hochard, Compression Characterization of High-modulus Carbon Fibers, Journal of Composite Materials 39 (1) (2005) 35–49. doi:10.1177/0021998305046433.
URL http://journals.sagepub.com/doi/10.1177/0021998305046433
[29] R. Kim, A. S. Crasto, Longitudinal Compression Strength of Glass Fiber-Reinforced Composites, Journal of Reinforced Plastics and Composites 13 (4) (1994) 326–338. doi:10.1177/073168449401300404.
URL http://journals.sagepub.com/doi/10.1177/073168449401300404
[30] F. Mujika, On the difference between flexural moduli obtained by three-point and four-point bending tests, Polymer Testing 25 (2) (2006) 214–220. doi:10.1016/j.polymertesting.2005.10.006.
URL https://linkinghub.elsevier.com/retrieve/pii/S0142941805001698
[31] F. Mujika, A. Arrese, I. Adarraga, U. Oses, New correction terms concerning three-point and four-point bending tests, Polymer Testing 55 (2016) 25–37. doi:10.1016/j.polymertesting.2016.07.025.
URL https://linkinghub.elsevier.com/retrieve/pii/S0142941816305232